Impact of clay coating on sandstone reservoir quality: A multiphase-field investigation by numerical simulation

KUMAR Akash[1, 2, *], SPÄTH Michael[1], PRAJAPATI Nishant[1], BUSCH Benjamin[3], SCHNEIDER Daniel[1, 4], HILGERS Christoph[3], NESTLER Britta[1, 2, 4]

1. Institute of Nanotechnology (INT), Karlsruhe Institute of Technology (KIT), Karlsruhe 76344, Germany;

2. Institute for Applied Materials - Microstructure Modelling and Simulation (IAM-MMS), Karlsruhe Institute of Technology (KIT), Karlsruhe 76131, Germany;

3. Structural Geology and Tectonics, Institute of Applied Geosciences (AGW-SGT), Karlsruhe Institute of Technology (KIT), Karlsruhe 76131, Germany;

4. Institute for Digital Materials Science (IDM), Karlsruhe University of Applied Sciences, Karlsruhe 76133, Germany

Abstract: The presence of clay coatings on the surfaces of quartz grains can play a pivotal role in determining the porosity and permeability of sandstone reservoirs, thus directly impacting their reservoir quality. This study employs a multiphase-field model of syntaxial quartz cementation to explore the effects of clay coatings on quartz cement volumes, porosity, permeability, and their interrelations in sandstone formations. To generate various patterns of clay coatings on quartz grains within three-dimensional (3D) digital sandstone grain packs, a pre-processing toolchain is developed. Through numerical simulation experiments involving syntaxial overgrowth cementation on both single crystals and multigrain packs, the main coating parameters controlling quartz cement volume are elucidated. Such parameters include the growth of exposed pyramidal faces, lateral encasement, coating coverage, and coating pattern, etc. The coating pattern has a remarkable impact on cementation, with the layered coatings corresponding to fast cement growth rates. The coating coverage is positively correlated with the porosity and permeability of sandstone. The cement growth rate of quartz crystals is the lowest in the vertical orientation, and in the middle to late stages of evolution, it is faster in the diagonal orientation than in the horizontal orientation. Through comparing the simulated results of dynamic evolution process with the actual features, it is found that the simulated coating patterns after 20 d and 40 d show clear similarities with natural samples, proving the validity of the proposed three-dimensional numerical modeling of coatings. The methodology and findings presented contribute to improved reservoir characterization and predictive modeling of sandstone formations.

Key words: quartz cementation; clay coating; grain coating; phase-field modeling; sandstone; reservoir quality; quartz overgrowth

Introduction

Reservoir quality of sandstones is crucial for hydrocarbon and geothermal resource exploration. It is highly dependent on grain size and detrital composition [1]. However, compaction, cementation, and dissolution during diagenesis can alter these initial controls. Nucleation discontinuities, or grain coatings, can reduce syntaxial overgrowth cements, thus preserving reservoir quality. Grain coatings maintain intragranular porosity in deeply buried sandstones by inhibiting quartz overgrowth cementation [2–3], and affect permeability based on their texture [4].

Clay mineral grain coatings are classified by texture (tangential or radial) and formation time (detrital or authigenic), with properties changing during diagenesis and clay mineral recrystallization [5]. Tangential clay mineral coatings often appear at grain contacts, suggesting pre-compaction emplacement. Radial clay mineral coatings usually result from diagenetic formation on detrital grains or tangential clay phases [6], but can also occur in

* **Corresponding author.** E-mail: akash.kumar@kit.edu

recent sedimentary deposits [7–8], linked to near-surface diagenetic processes in the phreatic zone [9].

Grain coating coverage on sandstone samples reduces quartz cement content due to decreased surface area for precipitation, as evidenced by natural samples and simulations [10–11]. Quantification of this coverage has been conducted on rock samples [8, 12–13], experimental datasets [14], and cores [11, 15–16], indicating a consistent correlation between grain coating coverage and syntaxial overgrowth cement reduction [11, 15, 17–20]. The effect of grain coating on quartz cementation is not dependent on specific clay mineral types, as both chloritic [11] and illitic coatings [20] demonstrate similar negative correlations with quartz cement volumes. This study neglects the effect of clay minerals on the model's applicability.

Numerical methods are crucial for studying how various rock properties affect key reservoir quality parameters in sandstones [10, 21–22]. Lander et al. [10] conducted simulation studies alongside laboratory experiments on quartz cement growth to comprehend the effects of grain size, polycrystallinity, and clay coatings on growth rates and cement volumes. They employed a continuous value cellular automata approach for simulating quartz nucleation and growth by Prism2D software. Their 2D simulations successfully captured quartz growth trends and realistic textures on clay-coated surfaces with certain limitations. 2D simulations, though computationally efficient, oversimplify important aspects. They restrict crystal rotation to in-plane movements, inaccurately represent fluid flow properties, and allow crystal contact points to completely block flow, unlike in 3D. 3D simulations offer a more realistic representation of natural rock structures by allowing heterogeneous crystallographic orientations and providing accurate predictions of fluid flow properties. These advantages make 3D simulations more suitable for comprehensive analysis of reservoir rock characteristics.

Prajapati et al. [21–22] conducted extensive 3D computational investigations using the multiphase-field (MPF) method to simulate syntaxial overgrowth cementation and analyze its impact on porosity-permeability relationships in sandstones. These studies successfully recreated realistic quartz cement textures in mono- and polycrystalline sandstones and recovered porosity-permeability relationships. However, Prajapati et al. [22] did not comprehensively analyze how clay coatings affect syntaxial quartz cementation and its subsequent impact on reservoir characterization. The MPF model has demonstrated promising capabilities in modeling various mineral growth and dissolution processes, including quartz cement growth [22–25], calcite precipitation [26–27], potash alum precipitation [26–27], and quartz crystal dissolution such as faceted crystal dissolution [28] and etch-pitting [29]. These studies and applications highlight the versatility and potential of the MPF model in simulating complex geological processes.

Authigenic clay mineral coatings can evolve dynamically from poorly to completely grain-coated textures, mirroring natural processes during sediment deposition, diagenesis [30], and clay mineral recrystallization [5]. In recent years, the MPF method has been used to address nucleation discontinuities by reducing growth rates of grains assumed to have coatings, based on the observation that coatings impede quartz grain growth [26, 31]. However, this method was relatively simplistic and not entirely accurate. The present work extends the computational investigations of Prajapati et al. [21–22] to examine the influence of clay coatings (nucleation discontinuities) on quartz cementation, porosity, permeability, and their interrelationships in sandstones using an MPF model. The investigation begins by validating the MPF model with nucleation discontinuities through simulations replicating quartz crystal patterns from Lander et al.'s [10] "quartz plate" experiments and reference samples. Natural examples of illitic grain coatings from the Permian Rotliegendes and Triassic Buntsandstein formations are used to evaluate their influence on inhibiting syntaxial quartz cementation, without considering their impact on compactional porosity loss. A numerical methodology is developed using the in-house solver PACE3D [32] to generate clay-coated grains, and systematic experiments on quartz cementation in digital clay-coated quartz crystals and multigrain packs are conducted by varying coating parameters individually. Fluid flow simulations in progressively cemented multigrain packs are conducted to compute permeabilities of samples with tangential clay coatings. The resulting datasets are analyzed to understand how these parameters impact cement volumes, porosity, permeability, and their interrelationships.

This research has significant implications for natural resource exploration and production. Our study enhances the understanding of clay coating effects on reservoir quality across diverse geological settings, offering a sophisticated framework for predicting reservoir properties in undrilled sections globally. It improves the assessment of potential hydrocarbon and geothermal resources in various sedimentary basins and refines diagenetic process modeling. By combining numerical simulations with observations from natural samples, we provide a comprehensive approach to understanding clay coatings' role in reservoir quality. This work advances sedimentary geology and offers practical applications in reservoir characterization and resource exploration worldwide.

1. Geological samples

This study used a suite of natural samples from the Permian Rotliegendes in northern-central Germany and the UK [15, 17–18] and from the Triassic Buntsandstein in

south-western Germany and eastern France [19, 33], as shown in Fig. 1. Although the burial histories vary largely between the study areas [20], the effects of nucleation discontinuities on syntaxial overgrowth cements are comparable. The samples from the Triassic Buntsandstein (max. burial depth of 2 200 m, max. temperature of 118 °C) and the Permian Rotliegendes (max. burial depth of 4 800 m, max. temperature of 178 °C) contain both tangential and radial illite grain coating textures (Fig. 1). The observed grain coating coverage ranges from 10% to 95% and syntaxial quartz cement contents range from 0.3% to 22.3%. Furthermore, samples were selected for evaluating the grain coating coverage rate in contact with the intergranular volume [18] and capturing the effect of grain

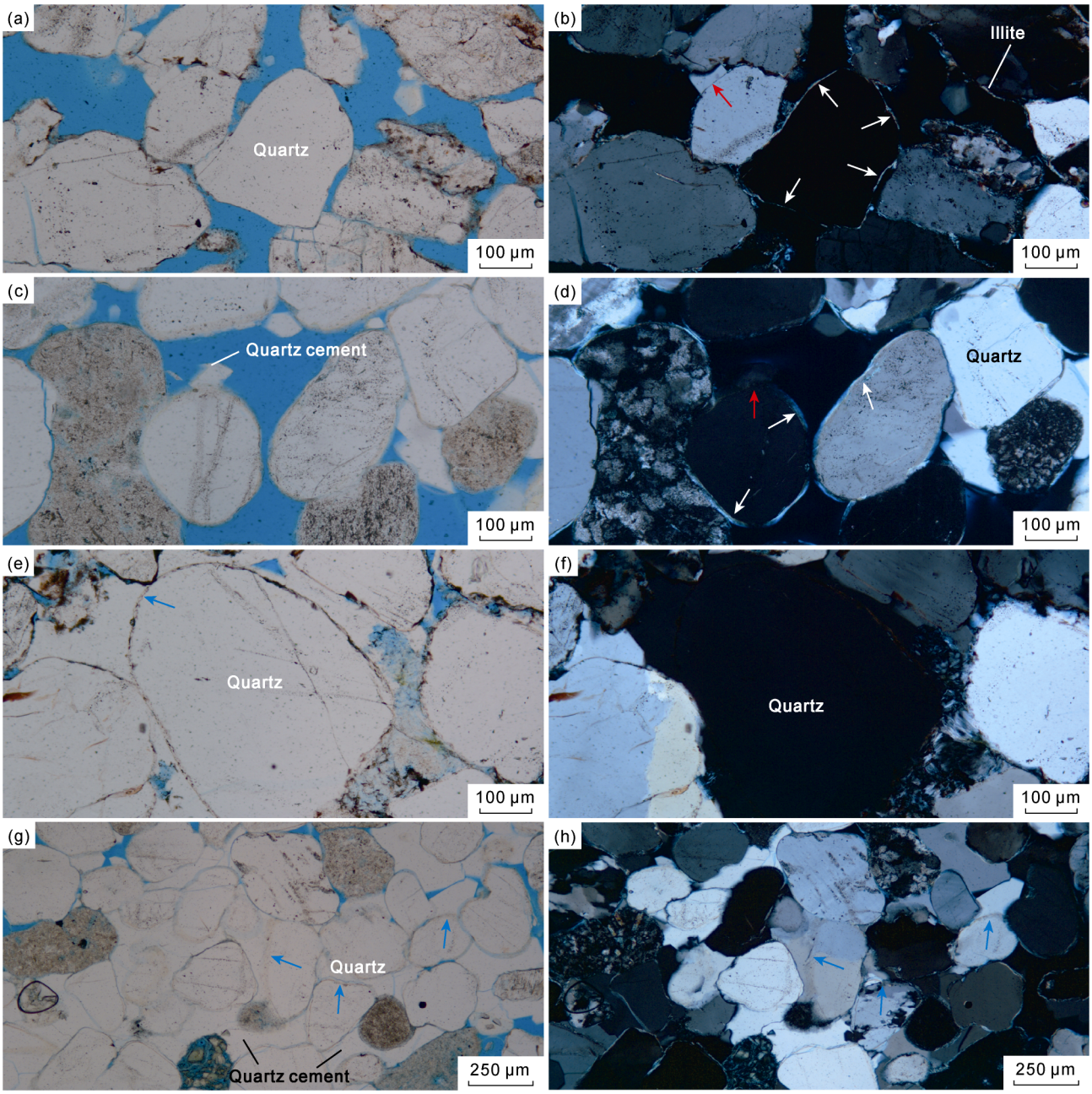

Fig. 1. Thin section images highlighting the effect of grain coating coverage on quartz cement content. (a), (b): Samples from Triassic Buntsandstein in the Upper Rhine Graben of south-western Germany and on the shoulders of its surrounding grabens, showing that grains completely coated by illite (white arrows) are lacking syntaxial quartz overgrowth cements, whereas grains which are incompletely coated (red arrow) are substrates for syntaxial overgrowth cements, with abundant intergranular pores preserved; (c), (d): Samples from Permian Rotliegendes in the North German Basin, showing that grains completely coated by illite (white arrows) are lacking syntaxial quartz overgrowth cements, whereas grains which are in-completely coated (red arrow) are substrates for syntaxial overgrowth cements, with abundant intergranular pores pre-served; (e), (f): Samples from Triassic Buntsandstein in the Upper Rhine Graben of south-western Germany, showing that incomplete (pigmented) hematite grain coatings (blue arrow) do not inhibit syntaxial quartz cement precipitation, and in-tergranular porosity is less than that in samples with well grain coated; (g), (h): Samples from Permian Rotliegendes in the North German Basin, showing that incomplete (pigmented) hematite grain coatings (blue arrow) do not inhibit syntaxial quartz cement precipitation.

coatings on nucleation discontinuities. Available data for the Permian Rotliegendes in the North Sea show that the SiO_2 content ranges from 0.45% to 1.69% [34]. The SiO_2 content for the Triassic Buntsandstein in the Upper Rhine Graben [36] ranges from 1.13% to 2.79% [35] if the measured SiO_2 contents are related to SiO_2 saturation calculations based on the findings of Manning et al. [35].

As natural samples often contain multiple mineral phases, the specific influence of individual mineral species on the overall properties of the reservoir can hardly be assigned. Present parameter and simulation studies may aid in assessing the specific influence of mineral species and paragenetic interactions to better understand natural systems.

2. Methods

Based on the work of Nestler et al. [37], this section explains the mathematical equations governing the MPF model for syntaxial overgrowth cementation in quartz sandstones, which was also previously utilized by Prajapati et al. [24] and Späth et al. [28]. This section also discusses the preprocessing workflow developed to model clay coatings on quartz grains in 3D digital sandstones, and describes the equations of the fluid flow model for the permeability calculations.

2.1. Multiphase-field model for syntaxial quartz cementation

We consider a physical domain Ω comprising N–1 solid phases (each representing a quartz grain) and a fluid phase (SiO_2 supersaturated), using a tuple of phase fields $\boldsymbol{\phi}(x,t)=[\phi_1(x,t), \ldots, \phi_N(x,t)]$. $\phi_\alpha(x,t)$ describes the presence of phase $\alpha\in[1, 2, \ldots, N]$ at $x\in\Omega$ and time $t\in\mathbb{R}_0^+$, $\phi_\alpha\in[0,1]$. The interface between grains or between a grain and liquid is represented by a diffuse region with a finite width. Within this interfacial region shared by grain α and the liquid or other grains, the phase-field parameter ϕ_α transitions smoothly from 0 outside the grain to 1 inside it. The grain's shape and location are determined by the isoline where ϕ_α=0.5. As a convention, the last phase $\alpha=N$ corresponds to the fluid phase. The Helmholtz free energy F of the system is given by:

$$F(\boldsymbol{\phi},\nabla\boldsymbol{\phi}) = F_{\text{bulk}} + F_{\text{intf}} = \int_\Omega \left[f_{\text{bulk}}(\boldsymbol{\phi}) + \varepsilon a(\boldsymbol{\phi},\nabla\boldsymbol{\phi}) + \frac{1}{\varepsilon}\omega(\boldsymbol{\phi}) \right] \mathrm{d}\Omega \tag{1}$$

F as the sum of the bulk F_{bulk} and interfacial F_{intf} energy contributions. $f_{\text{bulk}}(\phi)$ represents the bulk free energy density, given by:

$$f_{\text{bulk}}(\boldsymbol{\phi}) = \sum_{\alpha=1}^{N} f_\alpha h(\phi_\alpha) \tag{2}$$

As the interpolation of the phase-specific free energy density f_α using the interpolation function $h(\phi_\alpha)=\phi_\alpha$. The difference in the free energy densities between the solid and fluid phases creates a driving force for the interfaces and henceforth, provides the chemical driving force for the growth of quartz cement. The second and third terms in Eq. (1) denote the gradient $\varepsilon a(\boldsymbol{\phi},\nabla\boldsymbol{\phi})$ and potential $\omega(\boldsymbol{\phi})/\varepsilon$ energy density, collectively representing the interfacial energy density. ε is the length scale parameter that controls the width of the diffuse interface. The gradient energy density serves as an energetic penalty associated with the development of diffuse interfaces and is mathematically expressed by:

$$\varepsilon a(\boldsymbol{\phi},\nabla\boldsymbol{\phi}) = \varepsilon \sum_{\alpha=1}^{N}\sum_{\beta=1}^{N} \gamma_{\alpha\beta} a_{\alpha\beta}^2(\boldsymbol{\phi},\nabla\boldsymbol{\phi}) \left|\boldsymbol{q}_{\alpha\beta}\right|^2 \quad (\alpha<\beta) \tag{3}$$

where $\gamma_{\alpha\beta}$ denotes the interfacial energy of the α-β interface and $\boldsymbol{q}_{\alpha\beta}$ represents a generalized gradient vector, orthogonal to the α-β interface. Quartz crystals display diverse growth patterns influenced by their geochemical and physical growth environments. To accurately simulate these faceted crystals with distinct edges and corners, we employ a strongly anisotropic faceted-type surface energy, defined by a piecewise function. The formation of crystal facets is modeled using the anisotropy function $a_{\alpha\beta}(\boldsymbol{\phi},\nabla\boldsymbol{\phi})$ of the form:

$$a_{\alpha\beta}(\boldsymbol{\phi},\nabla\boldsymbol{\phi}) = \max_{1\le k\le n_{\alpha\beta}} \hat{\boldsymbol{n}}_{\alpha\beta}\,\boldsymbol{\eta}_{k,\alpha\beta} \tag{4}$$

where $\hat{\boldsymbol{n}}_{\alpha\beta}=\boldsymbol{q}_{\alpha\beta}/\left|\boldsymbol{q}_{\alpha\beta}\right|$ being the interface normal vector and $\boldsymbol{\eta}_{\alpha\beta}$ is the set of the position vectors corresponding to the corners of the capillary anisotropy Wulff shape of the α-β interface. The aforementioned surface energy anisotropy formulation offers a versatile framework for simulating faceted crystals of various shapes in both two and three dimensions. The potential energy density component establishes a barrier that prevents spontaneous phase transitions when interfacial driving forces are absent. For this work, we chose a multi-obstacle type potential energy density of the form:

$$\frac{1}{\varepsilon}\omega(\boldsymbol{\phi}) = \begin{cases} \dfrac{1}{\varepsilon}\left(\dfrac{16}{\pi^2}\sum_{\alpha\beta}\gamma_{\alpha\beta}\phi_\alpha\phi_\beta + \sum_{\alpha\beta\delta}\gamma_{\alpha\beta\delta}\phi_\alpha\phi_\beta\phi_\delta \right) & \boldsymbol{\phi}\in G \\ \infty & \boldsymbol{\phi}\notin G \end{cases} \tag{5}$$

The implication of multi-obstacle type potential energy density results in sharp energetic minima for the bulk phases through the Gibbs simplex condition as shown in Eq. (6).

$$G = \boldsymbol{\phi}\in\mathbb{R}^N \,|\, \left\{ \sum_{\alpha=1}^{N}\phi_\alpha = 1 \text{ and } \phi_\alpha \ge 0 \right\} \tag{6}$$

The term proportional to $\phi_\alpha\phi_\beta\phi_\delta$ prevents the occurrence of spurious third phase in binary interfaces. The governing evolution equation for phase-fields which provides the local minimization of the free energy is determined by the variational derivation of the energy functional. To address the varying growth rates of different phases without encountering interpolation issues in multi-phase regions, we utilize the formulation proposed by Steinbach et al. [38]. This approach allows us to assign distinct mobilities (growth velocities) to each phase. The

evolution equation is:

$$\frac{\partial \phi_\alpha}{\partial t} = -\frac{1}{N\varepsilon}\sum_{\substack{\beta=1 \\ \beta\neq\alpha}}^{N}\left\{M_{\alpha\beta}\left(\hat{\boldsymbol{n}}\right)\left[\frac{\delta F_{\text{int f}}}{\delta\phi_\alpha}-\frac{\delta F_{\text{int f}}}{\delta\phi_\beta}-\frac{8\sqrt{\phi_\alpha\phi_\beta}}{\pi}\left(\frac{\delta F_{\text{bulk}}}{\delta\phi_\beta}-\frac{\delta F_{\text{bulk}}}{\delta\phi_\alpha}\right)\right]\right\}$$

$$\alpha = 1\ldots N. \tag{7}$$

The mobility coefficient $M_{\alpha\beta}\left(\hat{\boldsymbol{n}}\right)$ of the α-β interface determines the interfacial kinetics, and is expressed as:

$$M_{\alpha\beta}\left(\hat{\boldsymbol{n}}\right) = M_{0,\,\alpha\beta}a_{\text{kin},\,\alpha\beta}\left(\hat{\boldsymbol{n}}\right) \tag{8}$$

where $M_{0,\,\alpha\beta}$ accounts for the difference in attachment kinetics, $a_{\text{kin},\,\alpha\beta}\left(\hat{\boldsymbol{n}}\right)$ considers the orientation dependency of growth rates, which is given by:

$$a_{\text{kin},\,\alpha\beta}\left(\hat{\boldsymbol{n}}\right) = \left\{1+\delta\left[\max_k\left(\hat{\boldsymbol{n}}\cdot\boldsymbol{\eta}_{\text{kin},\,k}\right)-\max_{k-1}\left(\hat{\boldsymbol{n}}\cdot\boldsymbol{\eta}_{\text{kin},\,k}\right)\right]\right\}\cdot \max_k\left\{\hat{\boldsymbol{n}}\cdot\boldsymbol{\eta}_{\text{kin},\,k}\right\}\ (k=1,\,2,\,\ldots,\,n_{\text{kin}}) \tag{9}$$

According to Wendler et al.[23], this function accounts for the faster pre-faceting quartz growth tendencies through the anisotropy strength parameter δ and different relative growth velocities of the different facets through the set of position vectors $\boldsymbol{\eta}_{\text{kin},\,k}$ of the corners of the kinetic anisotropy shape. The model equations are implemented within the parallel Multiphysics computational framework called PACE3D. Detailed information on the optimization and parallelization strategies of PACE3D are shown in the work of Hötzer et al. [32]. The simulation parameter set utilized in the present work is given in Table 1. The dimensional values of the parameters in the table are adapted from Prajapati et al. [22]. The set of position vectors $\boldsymbol{\eta}_{\text{cap, k}}$ and $\boldsymbol{\eta}_{\text{kin, k}}$ for the capillary and kinetic anisotropy shape, respectively, are taken from Ref. [23].

2.2. Modeling clay-coating on quartz surface

The presence of clay minerals acts as a barrier at the interface between detrital quartz grains and intergranular pore space, thus inhibiting quartz overgrowth [40]. Therefore, we define clay mineral as an inert phase in our modeling framework. For generating digital clay-coatings with user-defined thickness, volume fraction and patterns (e.g. continuous, randomly distributed), a pre-processing workflow was developed in this work. It consists of the following steps:

In the first step, for the quartz grain phases in a computational domain, we generate full clay coating of a given thickness based on the values of phase-field ϕ_{grain} in the interface region (Fig. 2).

In the second step, we generate continuous (one-sided, layered) and random coatings by the following steps. Continuous coatings: For one-sided clay coatings (Fig. 2), substitute the clay phase in the user-defined regions separated by spatial planes with the liquid phase. Using user-defined spatial planes, layered coatings (Fig. 2) can be generated. Random coatings: For random patterns of clay coatings of a given volume fraction, an iterative pre-processing algorithm is developed. While the clay volume fraction is greater than a user-defined value, the following is needed to be executed: (1) Select a random spatial point in the clay phase of the numerical domain, which acts as the center of a sphere of user-defined radius. (2) Substitute the clay phase that occurs within this spherical region with the liquid phase. (3) Calculate the volume fraction of the clay coating in the entire domain. (4) If the volume fraction does not fall within the user-defined range, go to step (1); otherwise, exit the iterative loop.

With this workflow, coatings of different thicknesses, patterns and percentage coverages can be generated on grains of arbitrary realistic shapes. The generated clay-coated quartz grains in a computational domain filled with a liquid phase serve as the initial numerical setup for simulating anisotropic cement growth. Fig. 2 displays the generated random coating pattern on a grain with an irregular shape.

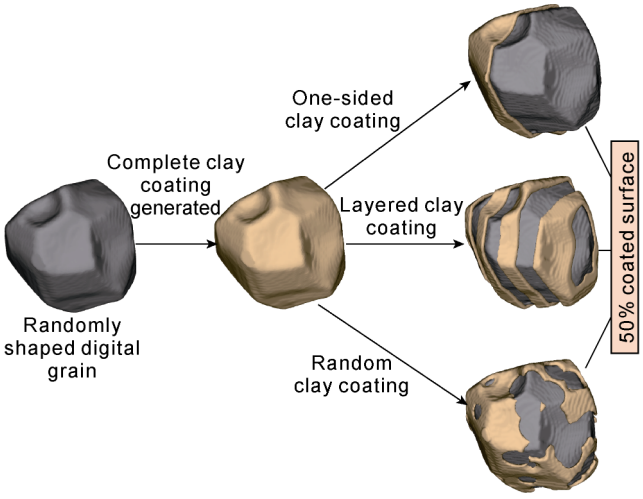

Fig. 2. Digital clay-coating workflow.

Table 1. Parameters used for MPF numerical simulations (adapted from Ref. [25])

Model parameter	Symbol	Non-dimensional value	Dimensional value
Grid cell size	Δx	0.5	0.5 μm
Time-step width	Δt	0.001 45	87.5 s
Quartz-liquid interface energy density	γ_{ql}	1	0.36 J/m^2
Clay-liquid interface energy density	γ_{cl}	0.03	0.010 8 J/m^2
Quartz-quartz interface energy density	γ_{qq}	1.91	0.687 6 J/m^2
Clay-clay interface energy density	γ_{cc}	0.42	0.151 2 J/m^2
Higher-order interface energy density	$\gamma_{\alpha\beta\delta}$	25	9 J/m^2
Length scale	ε	1.1	1.1 μm
Kinetic coefficient of the quartz-liquid interface	$\mu_{0,\,\text{ql}}$	1.0	4.65×10^{-17} m^4/(J·s)
Driving force for quartz cementation	Δf_{ql}	−0.294	-1.0×10^5 J/m^3
Kinetic anisotropy strength	δ	115	

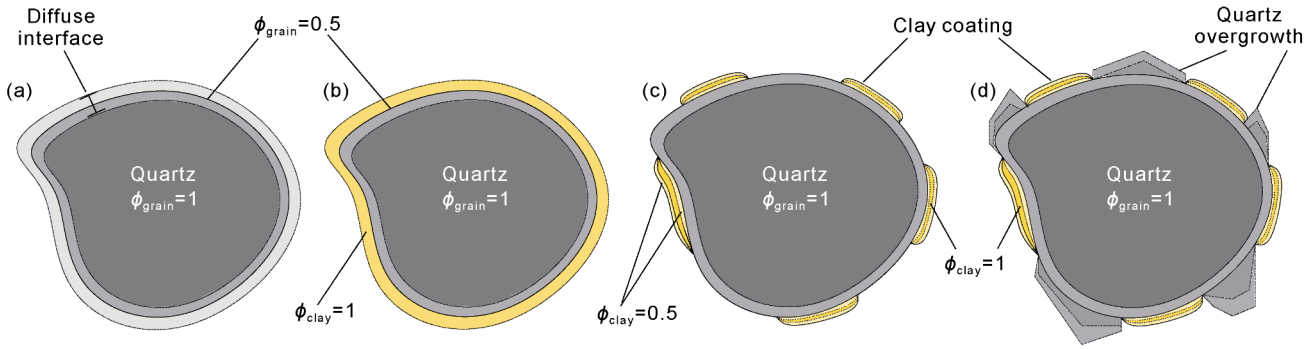

Fig. 3. Modeling work-flow schematics. (a) A randomly shaped grain. (b) Complete clay coating phase of a given thickness (denoted by ϕ_{clay}). (c) Coating pattern generated using the pre-processing workflow. (d) Simulated quartz overgrowth on the partially coated grain.

The inert clay phases are incorporated by immobilizing the clay-liquid interfaces. Numerically this translates to $M_{0,\mathrm{cl}}$ being the mobility coefficient of clay-liquid system. It essentially implies that the clay phase ϕ_{clay} does not evolve during quartz growth simulation, and as per the evolution equation, we have:

$$\frac{\partial \phi_{clay}}{\partial t} = 0 \tag{10}$$

Fig. 3 gives the schematic representation of the modeling workflow. Complete clay coating of a given thickness is generated on a grain using the contours of the phase-field parameter ϕ_{grain} in the diffuse interface region (Fig. 3a, 3b). Following this, a user-defined coating pattern is generated using the described pre-processing workflow (Fig. 3c). Finally, anisotropic quartz overgrowth is simulated using the MPF model (Fig. 3d).

2.3. Computational fluid dynamics model for permeability calculations

Computational fluid dynamics (CFD) analysis is employed to calculate the permeability of clay-coated sandstones at various stages of cementation. For this purpose, Stokes equations are employed, under the laminar flow assumption. The equations are mathematically expressed as:

$$\mu_{\mathrm{d}} \Delta \boldsymbol{u} - \nabla p = 0 \tag{11}$$

$$\nabla \cdot \boldsymbol{u} = 0 \tag{12}$$

A constant-pressure drop is applied in the x-direction, while all other boundaries are set to a free-slip boundary condition. The contact between the liquid and grain/clay systems has a no-slip boundary condition. The permeability K is calculated by the Darcy's law:

$$K = \frac{\mu_{\mathrm{d}} \overline{\boldsymbol{u}}}{\nabla p} \tag{12}$$

Non-dimensional parameters are adopted for the fluid flow simulations of our previous work, given the comparable domain size in the present and the previous work.

3. Results and discussion

In this section, we begin by validating our quartz growth model by replicating the crystal patterns observed in both previous laboratory experiments and our own natural samples. Following this validation, we explore the impact of coating parameters, such as orientation, percentage coverage, and pattern, on cement volumes through unconstrained single crystal growth simulations. Furthermore, we conduct a series of simulations in multi-grain packs with varying coating patterns and percentage coverage to analyze the resulting changes in cement volumes, porosity, and permeability. This innovative approach using the MPF method not only enhances our understanding of clay coatings' effects on reservoir properties but also holds significant promise for future research in reservoir characterization and resource exploration on an international scale.

3.1. Model validation with experiments and natural samples

3.1.1. Validation with experiments

Experimental investigations conducted by Lander et al. [10] showcased the impact of nucleation discontinuities on quartz overgrowth within a well-controlled laboratory environment. The experiments were conducted at a pressure of 69 MPa and temperatures ranging from 300 °C to 350 °C. Although the work of Lander et al. [10] did not provide specific information on SiO_2 concentration or saturation index related to quartz grain cementation, previous studies have shown that the saturation index in natural settings typically falls between 0.45 and 2.79 [34–36, 41]. This index is crucial in determining the rate at which equilibrium is achieved and directly influences the chemical driving force behind quartz cementation [22–23]. For quartz growth modeling, researchers often employ reasonable assumptions to reduce simulation time and computational costs, and simplify assumptions to optimize computational resources while maintaining the integrity of the simulated processes [21–23, 25]. This study employs simulation parameters for quartz growth similar to those used by Prajapati et al. [22]. In their work, the authors simulated digital quartz grain cementation under conditions of 44 MPa pressure, 150 °C temperature, and a saturation index of 6. The work of Wendler et al. [23] and

Prajapati et al. [22] provides valuable information on the reliability of these assumptions and their impact on the accurate replication of natural phenomena. By adopting similar simulation conditions and making informed assumptions, researchers can effectively simulate complex processes like quartz cementation while managing computational demands. This approach allows for the exploration of long-term geological processes within practical time-frames and resource constraints. Therefore, the assumption of fluids supersaturated with respect to SiO_2 is reasonable for the attempted simulations.

As a starting point, we validate our quartz cementation model that incorporates inert phases by simulating the quartz plate experiments in previous studies [10] and subsequently comparing our simulation results with the previous laboratory findings. For the reference, we consider the smallest copper grid experiment of Lander et al. [10], where square holes measuring 42 μm in side of the copper grid were separated by a distance of 20 μm. For the simulation, we recreate a specific portion of this experiment using a 3×3 mesh, as shown in Fig. 4a. The size of the simulation domain is $406\Delta x \times 650\Delta y \times 406\Delta z$ (with $\Delta x = \Delta y = \Delta z$ = 0.5 μm). In the y-direction, two solid layers of thickness 20 μm represent the quartz plate (in grey) and copper mesh (in copper) with square holes, respectively. The rest of the domain in y-direction was filled with the SiO_2-supersaturated liquid phase, which is not shown in Fig. 4a for the purpose of clear visualization. With this simulation setup, it was ensured that the hole dimension and grid spacing matched the reference experiments. The simulation results are very similar to the findings of Lander et al. [10] in crystal growth patterns (Fig. 4).

Using the parameters given in Table 1, a phase-field simulation of growing quartz crystals was performed. Fig. 4a depicts different stages of quartz overgrowth. As quartz cements grow in the holes, individual crystals with facets are formed in accordance with the euhedral shape. At a later stage, these individual crystals merge in a lateral direction owing to identical crystal orientation and faster growth in that direction (Fig. 4a). These simulation results show clear similarities with the overgrowths morphologies produced in the experiment, as depicted in Fig. 4. As previously mentioned, the temperature, pressure, and supersaturation conditions used in this simulation (from the work of Prajapati et al. [22]) differ from those in the experiments conducted by Lander et al. [10]. Our model demonstrates strong qualitative agreement with experimental observations, particularly in accurately reproducing the morphologies of quartz cementation. This alignment underscores the model's capability to capture essential aspects of the cementation process. While the absence of detailed concentration data from Lander et al. [10] precludes a direct quantitative comparison of quartz cement growth rates, our validation approach leverages the strength of morphological similarities, providing valuable insights into the model's predictive capabilities. The current validation lays a solid foundation for understanding quartz cementation processes. Prajapati et al. [22] and Wendler et al. [23] have demonstrated that the model works well for pure quartz systems.

However, validating the model with physical growth rates for quartz and clay setups (such as in the experiments

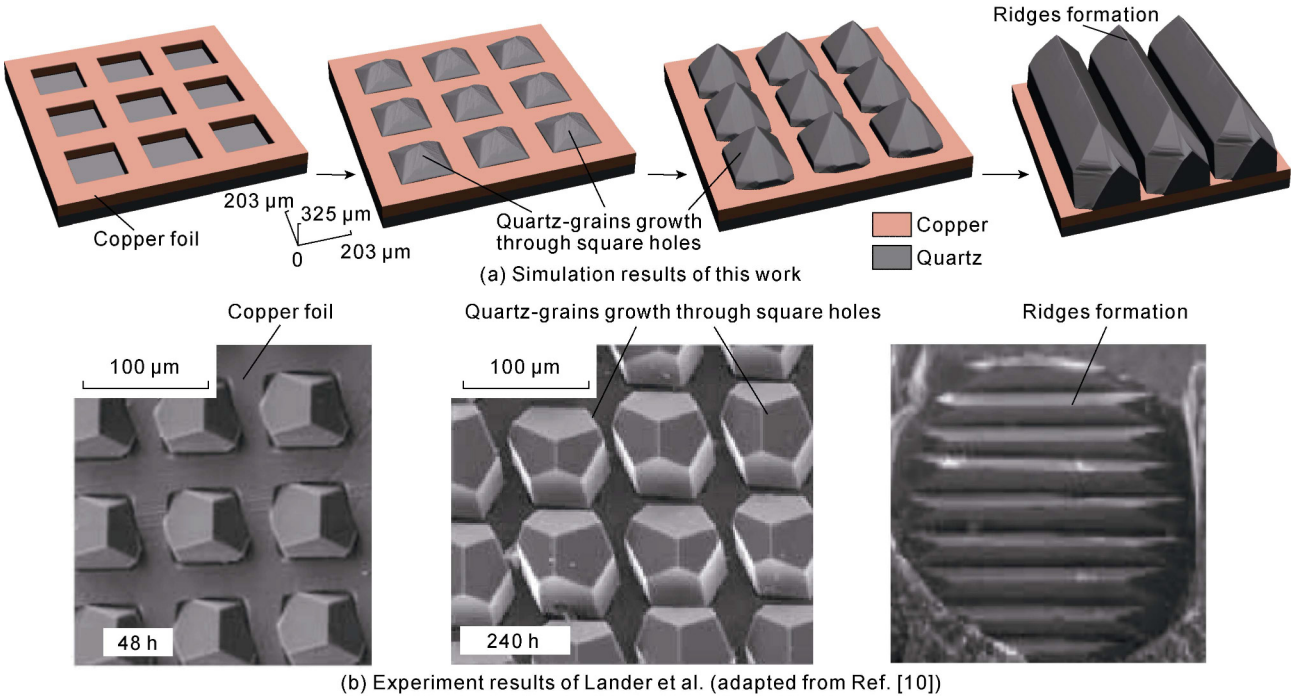

Fig. 4. Comparison of "quartz plate overgrowth" experiment by Lander et al. and simulation results generated using MPF method (this work).

of Lander et al. [10] where copper was used to simulate the clay minerals) presents challenges. In these experiments, supplementary minerals are added to increase growth rates, resulting in a multi-component fluid. Our current simulation uses a "pure" SiO_2 oversaturated liquid, making direct comparisons to these more complex experimental setups difficult.

While the MPF method is capable of simulating multi-component phenomena and varying concentrations, we did not chose it to incorporate these aspects in the current work due to computational costs. For coated quartz, limited quantitative data is available, and even in cases where data exists, the composition is often unspecified or too intricate for direct comparison. Given these constraints, we focused on a qualitative comparison, achieving a sound visible agreement with lab experiments. It's important to note that our current work, based on the dataset provided by Prajapati et al. [22], already establishes a robust framework well-accepted for reservoir quality characterization.

3.1.2. Validation with natural sample

In natural samples featuring partially coated grains, internal growth zonation is evident. Thin section microphotographs of a Buntsandstein sample, as shown in Fig. 5a, reveal areas of grain coating (indicated by red arrows) and clean grain surfaces (indicated by green arrows). Cold cathodoluminescence image of the same grain and overgrowth is presented in Fig. 5b. Within regions of incomplete grain coating coverage, syntaxial quartz overgrowth displays growth zonation (depicted by dark and bright blue colors, delineated by dashed red lines) before encasing the grain coating laterally. This analysis highlights, the evolution of pore surface roughness over geological time and additionally highlights the effect of nucleation discontinuities may have on reservoir utilization. Rather than one smooth crystal surface next to a pore, the small precipitates increase the pore surface roughness and may alter fluid production behavior [42]. In this study, the assumption of a higher supersaturation index accelerates the process by approximately tenfold, without altering other aspects of the natural phenomenon of quartz cementation.

To validate the model, we consider a similar grain surface with coated and clean surface in a simulation domain. The configuration comprises of a spherical quartz grain with a diameter of 100 µm featuring a random, partially coated surface, immersed in a supersaturated liquid phase, as depicted in the initial stage of Fig. 5c along the central 2D plane (liquid phase omitted for clarity). The dimension of the simulation domain is $300\Delta x \times 600\Delta y \times 300\Delta z$ (with $\Delta x = \Delta y = \Delta z = 0.5$ µm). The simulated quartz overgrowth (utilizing parameters given in Table 1) is shown in different shades of grey. Notably, initial precipitation occurs on uncoated sections of the grain, followed by lateral encasement of the grain coating phase, as also observed in the natural example. Unlike the natural sample, the simulated growth is unconstrained, resulting in facet formation at later stages.

3.2. Discussion

In this section, we explore how coating parameters affect the resulting cement volumes. We conduct simulations of overgrowth cementation on single grains with clay coatings under unconstrained conditions to investigate these influences. All the simulations are performed using the parameters given in Table 1.

3.2.1. Influence of crystallographic orientations of quartz grains on cement growth rate and volume of sandstone

The prismatic growth habit of quartz crystals involves

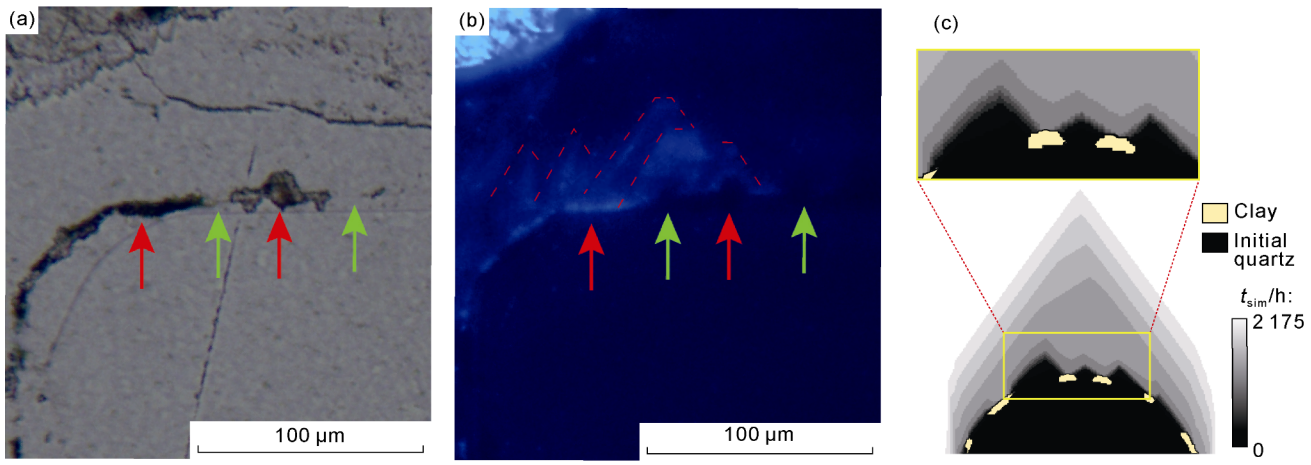

Fig. 5. Thin section microphotographs and phase-field simulation result of a Buntsandstein sample. (a) Partially coated quartz grain in a sample from the Buntsandstein, with grain coated areas (red arrows) and clean grain surfaces (green arrow) indicated. (b) Cold cathodoluminescence image of the same grain as in (a), showing a growth zonation of syntaxial quartz overgrowth (dark and bright blue colors, indicated by dashed red line) before laterally encasing the grain coating, in the area of the incomplete grain coating coverage. (c) Phase-field simulation result illustrating the evolution of internal growth zonation over time for a partially coated grain: the initial precipitation occurs on uncoated sections of the grain, followed by lateral encasement of the grain coating phases resembling the natural sample.

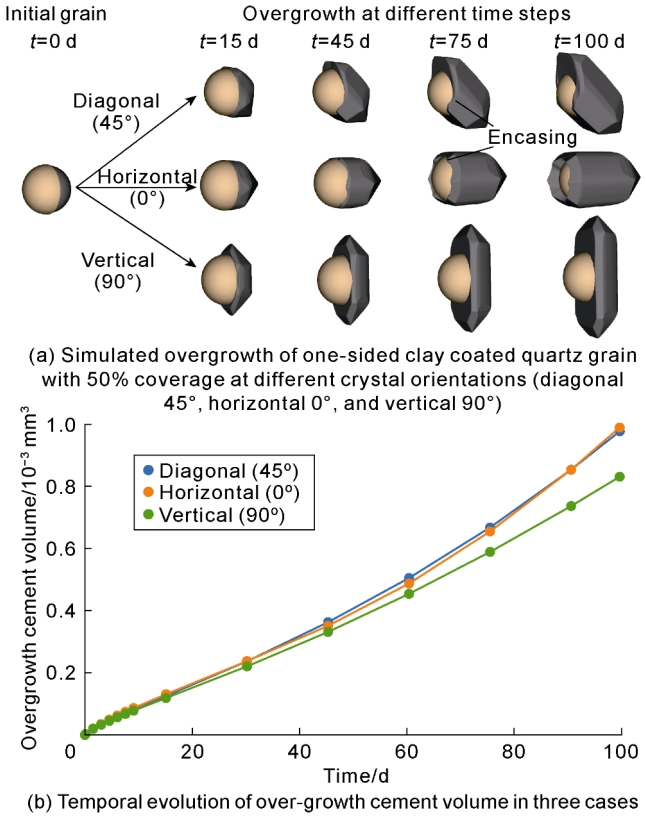

(a) Simulated overgrowth of one-sided clay coated quartz grain with 50% coverage at different crystal orientations (diagonal 45°, horizontal 0°, and vertical 90°)

(b) Temporal evolution of over-growth cement volume in three cases

Fig. 6. Evolution of quartz overgrowth and cement volume over time at three orientations.

rapid growth along the c-axis until faceting is complete. Upon faceting, the pyramidal and prismatic facets develop in their euhedral form. Previous studies have shown that pyramidal facets tend to grow at faster rates compared to prismatic facets [10]. These growth tendencies of quartz are incorporated in Refs. [22–23]. Utilizing the digital preprocessing workflow detailed above, spherical grains with a continuous one-sided coating, covering 50% of their surface, and with a diameter of 100 μm, were generated within sufficiently large simulation domains for cement growth (Fig. 6). Three distinct c-axis orientations of the quartz substrate grain in relation to the clay coated surface, namely horizontal (0°), vertical (90°) and diagonal (45°), were investigated. The resulting simulated overgrowths and temporal evolution of cement volume over time are depicted in Fig. 11. The observed growth rate of cement is lowest in the vertical orientation. For the diagonal and horizontal orientations, an intriguing dynamic between time and cement volume is noted. During the early stages (up to t_{sim} = 40 d), the cement volumes for both diagonal and horizontal orientations show little difference, as both develop euhedral shapes. By t_{sim} = 45 d, the appearance of additional pyramidal facets through lateral encasement in the diagonal orientation results in an accelerated growth rate for this orientation.

Subsequently, at t_{sim} = 75 d, lateral encasement with an increased presence of rapidly growing pyramidal faces is also observed in the horizontal orientation, thus enhancing the cement growth rate. Consequently, by the end of the simulation period (t_{sim} = 100 d), the grain having a horizontally oriented c-axis accumulates a greater volume of cement. This simulation study uncovers a fascinating interplay between the growth of exposed pyramidal faces and the emergence of new pyramidal facets through lateral encasement.

3.2.2. Influence of coating coverage on cement growth rate and volume of sandstone

The simulations were conducted under an assumption that a digital spherical quartz grain with size 92 μm and random shape in a sufficiently large simulation domain, and under a precondition that three distinct clay coatings for the same digital grain shape with varying coating coverage (i.e. 20%, 50%, and 80% of surface area) are generated. The quartz grains' growth orientation is illustrated in Fig. 7. Subsequently, quartz overgrowth was simulated using the parameters given in Table 1. The simulated overgrowth for the three cases is depicted in Fig. 7a. As anticipated, grains with lower coating percentage coverage exhibit greater cement volumes compared to those with higher percentage coverage. The temporal evolution of cement volume is illustrated in Fig. 7a for all three cases. Decreasing the percentage of clay coating coverage results in increased cement volume and growth rate, which is attributed to a larger available surface area for cement growth in less coated ones. Additionally, these plots display non-linear behavior during the initial overgrowth phase (approximately until t_{sim}= 2 d, i.e., the facet formation phase). Once all facets have fully formed on the quartz surface, the growth proceeds linearly until t_{sim}= 30 d (Fig. 7a). However, Fig. 7b suggests that if the simulation had run for longer than 30 d, the non-linear behavior of the cement overgrowth would have become evident in Fig. 7a. This inference is supported by the "randomly coated" grain curve in Fig. 7b, which matches the "50% clay-coating" curve in Fig. 7a. Due to the significant computational cost, further analysis beyond t_{sim}= 30 d was not conducted for the first case, focusing on the influence of coating coverage.

3.2.3. Influence of coating pattern on cement growth rate and volume of sandstone

In order to comprehend how the coating pattern on quartz grains impacts the cement growth and volume, three different patterns with 50% coverage each were investigated. The left plot of Fig. 7b illustrates the initial stage. For simplicity, we refer to these patterns as layered coated, randomly coated, and half coated. The model parameters are provided in Table 1, and the results are depicted in Fig. 6. The temporal evolution of cement volume is plotted in Fig. 6b. It is observed that in the

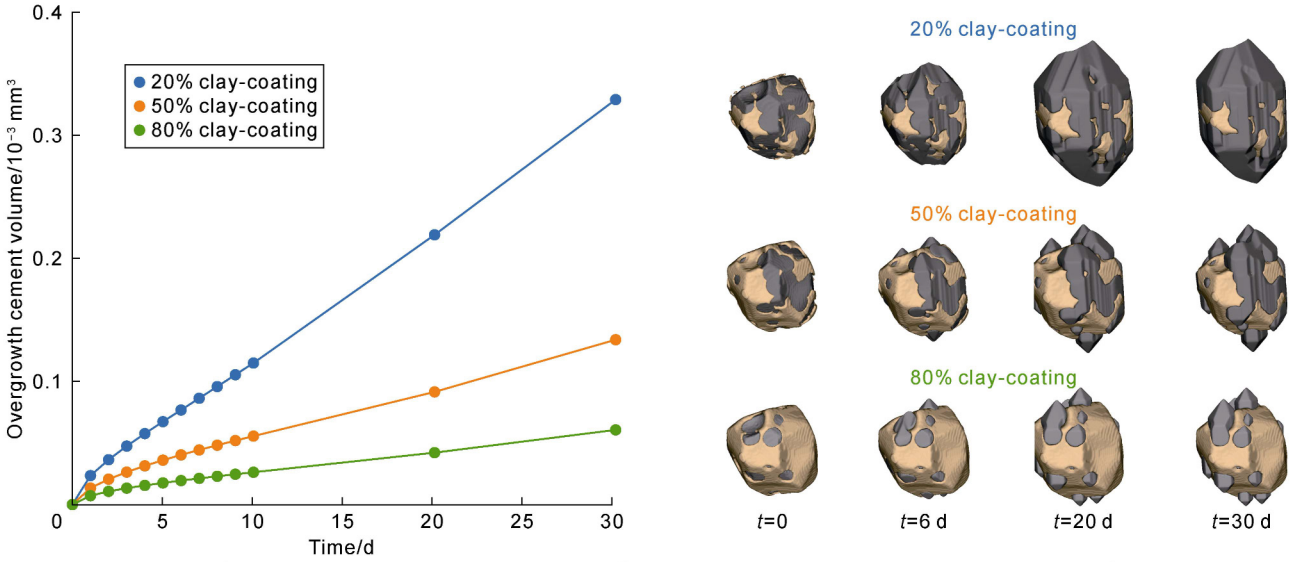

(a) Simulated overgrowth on a quartz grain of arbitrary shape, showing the temporal evolution of overgrowth cement volume for different coating coverages

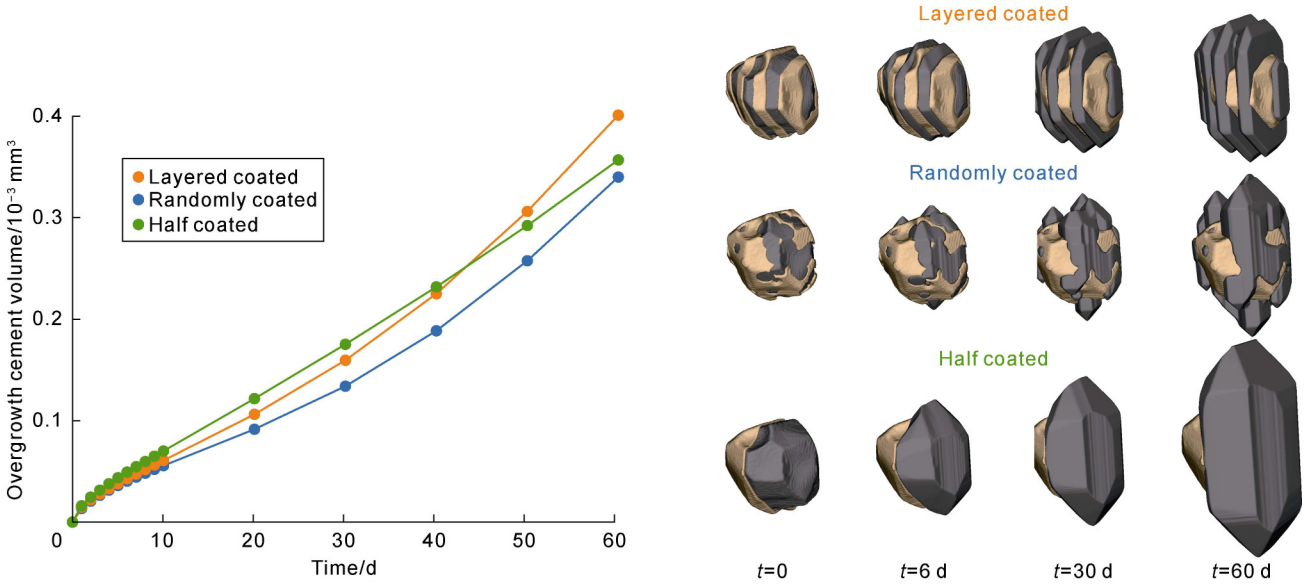

(b) Simulated overgrowth on a quartz grain with a coverage of 50%, showing the temporal evolution of cement volume for different coating patterns (randomly, layered and half coated)

Fig. 7. Simulated overgrowth on a quartz grain of arbitrary shape over time.

initial to intermediate stages (t_{sim} of 0–20 d), the cement volumes increase in a similar range. At later stages (after 30 d), when facet formation is complete, depending upon the presence of faster growing free faces, further growth differences occur. For the layered coated grain, surface area of faster growing faces is higher than the other cases, thereby resulting in higher cement volumes towards the end of simulation (i.e. approx. around 60 d). These simulation results reveal that the influence of the coating pattern becomes more evident during later stages of overgrowth, particularly as flat faces emerge, encasing the coating laterally and continuing to expand. In the early stages, the effect of the coating pattern is relatively minor. Even though the surface area covered by a clay mineral coating is 50% in each case, the volume of precipitated quartz cement varies over time. Generally, the grains with random clay coatings exhibit lower amounts of quartz cement, likely because the uncoated areas where cement can form are smaller compared to the other cases. This demonstrates that larger uncoated areas correspond to higher amounts of overgrowth cement formation.

Cement growth was simulated for three random clay coating patterns with 50% coverage each. The model parameters are provided in Table 1, and the results are depicted in Fig. 8, revealing the temporal evolution of overgrowth cement. There is no noticeable difference in the increase of net cement volume among the three packs during the initial stages (i.e., t_{sim} of 0–25 d). However, a visible difference in net cement volumes emerges during the intermediate stages (t_{sim} of 25–100 d) as the effect of the coating pattern becomes more pronounced. Eventually, in later stages where the overgrowth completely occludes the pore space, the net cement volumes converge to the same value for the three cases.

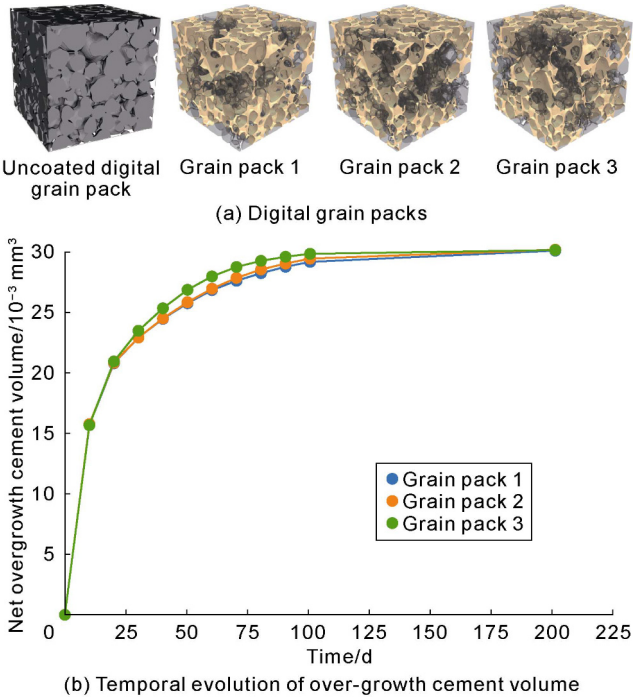

Fig. 8. Temporal evolution of overgrowth cement volumes for three coating patterns (digital grain packs used for generating three clay coating patterns with 50% coverage each).

3.2.4. Influence of coating on reservoir quality

A systematic simulation study is conducted to examine the influence of syntaxial overgrowth and clay coating coverage on the petrophysical properties, encompassing cement volume, porosity, permeability, and their interrelations. For the simulations, we consider a pack of digital sandstone in a computational domain of dimensions of $1\,000\Delta x \times 1\,000\Delta y \times 1\,000\Delta z$ ($\Delta x=\Delta y=\Delta z=0.5$ μm), as shown in Fig. 8 and Fig. 9. Both of the grain packs are exactly the same and comprise of 464 grains with random crystallographic orientations (Fig. 9), with the average grain size of 80 μm, and the initial porosity of 25%.

Three random clay coating patterns of varying coverage (i.e. 30%, 50%, and 70%) were generated on the digital grain packs, as shown in Fig. 9b. The distribution of clay phase is shown in Fig. 9b. Using the parameters given in Table 1, simulations were performed on the overgrowth at different stages of time for the three grain packs (Fig. 9c–9e). The pack with higher coating coverage undergoes less extensive cementation, and thereby exhibits higher pore space than others at all the stages. The difference in pore space is predominantly visible after 40 d of simulation. The resulting microstructures with clay-coating show similarities with natural samples in terms of cement overgrowth, pore space and clay coatings, as illustrated in Fig. 9a. The temporal evolution of cement volume and resulting porosity is respectively plotted in Fig. 10a and Fig. 10b. It is observed that the porosity reduces more rapidly in sandstones with lower coating coverage, due to higher surface area for cement growth, as also visible in the cement volume-time plot in Fig. 10a. Velocity streamlines depict fluid flow through the three packs with different coating coverages after approximately 10 d of cementation. Grain packs with higher coating coverages retain higher pore connectivity compared to those with lower coverages (Fig. 10e). This finding is also in agreement with field studies and experiments, showing generally higher permeability at same porosities in samples containing higher grain coating coverages [13]. However, this idealized correlation is seldom found in other natural sample series. This is due to the following factors: (1) other natural sample series contain other non-quartz cements occluding the pore space, (2) clay mineral coating textures (tangential, radial, or pore-bridging) also affect the permeability [4], and (3) illitic grain coatings have been shown to enhance pressure dissolution, further reducing porosity and permeability [17, 20].

Using the fluid-flow model elaborated in this work and flow parameters [22], computational fluid dynamics (CFD) analysis was performed on the packs at different stages of simulation. At the same porosity, sandstones with higher coating coverage are more permeable than those with lower coating coverage (Fig. 10c). For sandstones with higher coating coverage, the lesser amount of cements precipitate in the pore space, and vice versa. Consequently, these overgrowths can only block pore spaces in their immediate vicinity, whereas regions with clay coatings remain unaffected. Thus, sandstones with a larger coating coverage exhibit higher permeabilities, as illustrated in Fig. 10d and 10e.

The quartz overgrowth cement textures formed on uncoated or partially grain-coated samples may influence pore surface roughness, thereby affecting wetting properties and potentially impacting fluid production from the subsurface [41].

3.2.5. Comparison with natural samples

Datasets correlating the quartz cement content and coating coverage in natural sandstone samples, derived from previous field studies [15, 19–20], are available. Although the compiled sample series experienced different thermal histories and interacted with different fluids, a comparable correlation between grain coating coverage and quartz cement volume can be established. This supports the assessment that the grain coating coverage is a main controlling factor in controlling the available surface area for syntaxial quartz cement precipitation across multiple different study areas and their respective fluid and thermal histories. The simulation results after 20 d match the overall correlation of presented natural samples quite well (Fig. 11). Furthermore, samples experiencing higher thermal exposure, but similar fluids from the Buntsandstein in the Upper Rhine Graben show higher quartz cement contents at low grain coating coverage (less than

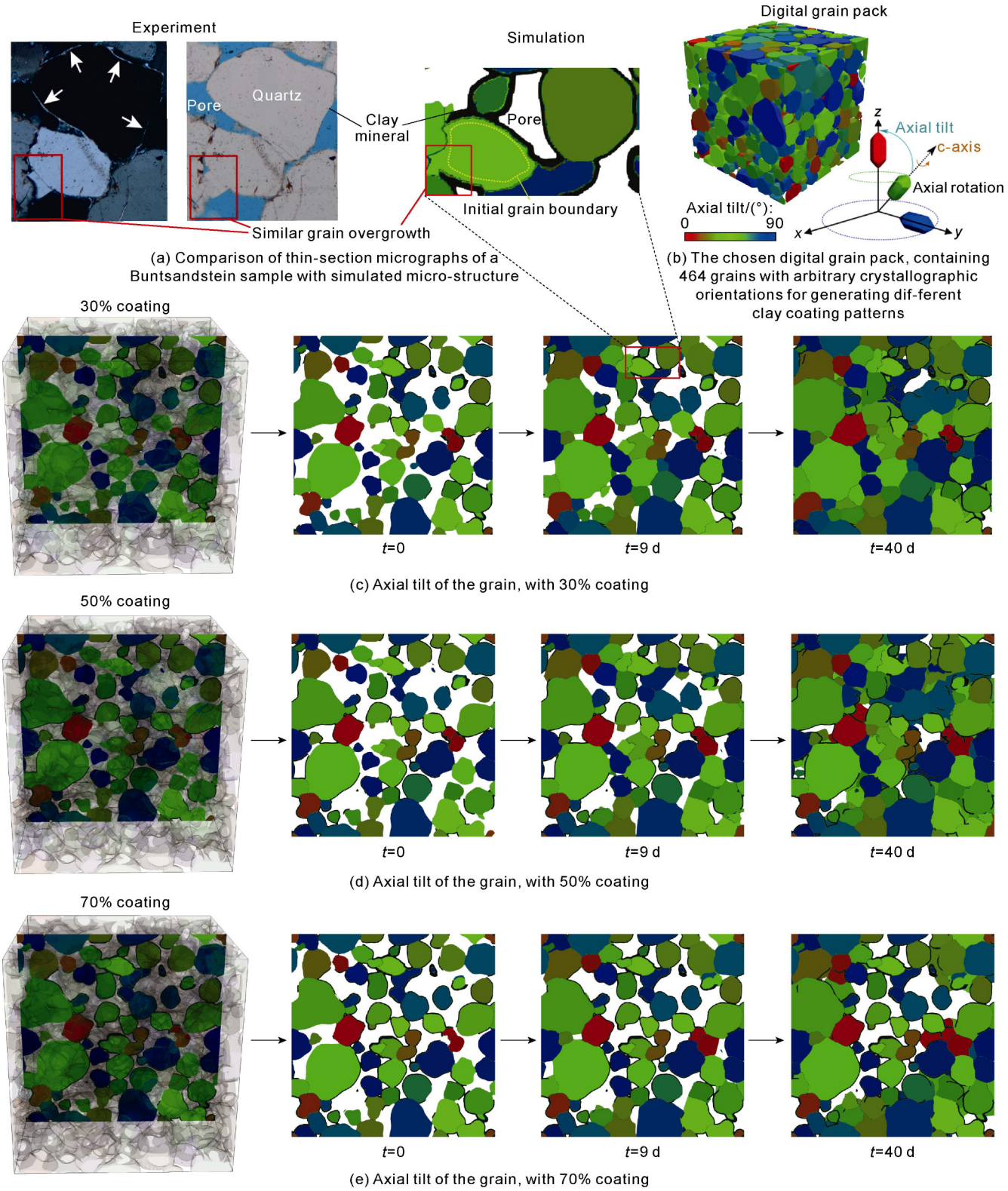

Fig. 9. Thin-section micrographs of a Buntsandstein sample and simulated influence of clay coating coverage on petrophysical properties.

40%) (orange diamonds in Fig. 11) than samples experiencing lower thermal exposures at the same grain coating coverage (red circles in Fig. 11). This behavior is matched by the simulation results after 40 d (red triangles in Fig. 11) compared to 20 d (purple triangles in Fig. 11), where higher thermal exposure also results in larger quartz cement volume. This demonstrates the efficacy of the modeling methodologies and digital work-flow presented herein, particularly in addressing the intricacies of cementation processes in clay-coated sandstone. These simulations therefore allow the pre-drill assessment of scenarios relating to variable grain coating coverages to

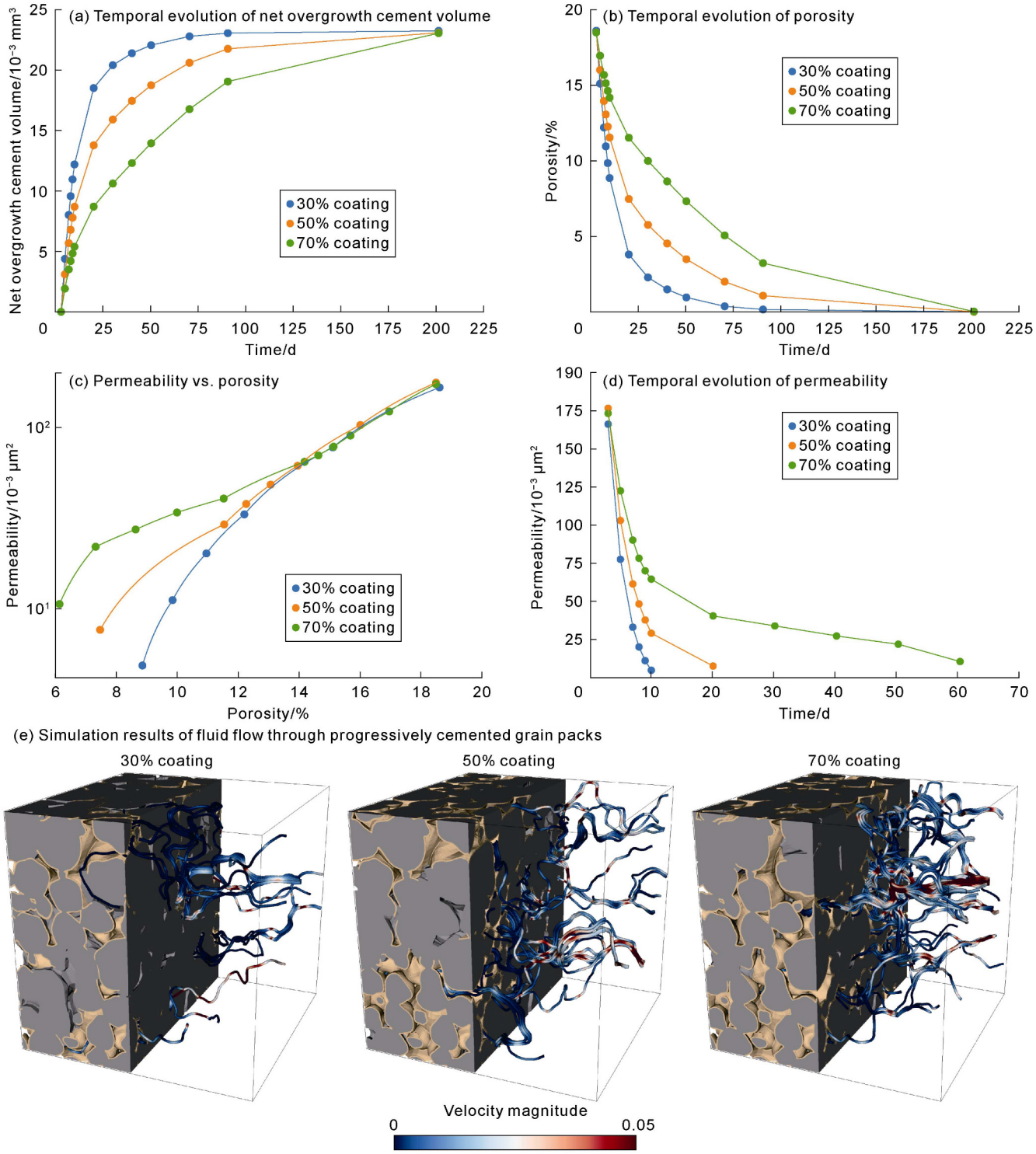

Fig. 10. Variation of net overgrowth cement volume, porosity and permeability of digital grain packs with different coating coverages.

assess likely overgrowth cement contents and derive porosities and permeabilities of prospective reservoir lithology as a function of thermal exposure. The integration with previously derived workflows for grain dissolution [29], mono- and polycrystalline quartz grains affecting overgrowth morphologies and volumes [21–22], fracture cementation formation [24, 26–27, 43] will be a valuable addition to pre-drill reservoir quality assessments using digital rocks.

4. Conclusions and outlook

This study reveals how clay coatings affect syntaxial overgrowth cementation and resulting reservoir properties in sandstones. The two innovative modeling aspects of this work are as follows: (1) Adaptation of a multi-phase-field model to incorporate inert phases analogous to clay coatings. This modeling approach is capable of replicating the overgrowth morphologies observed in the

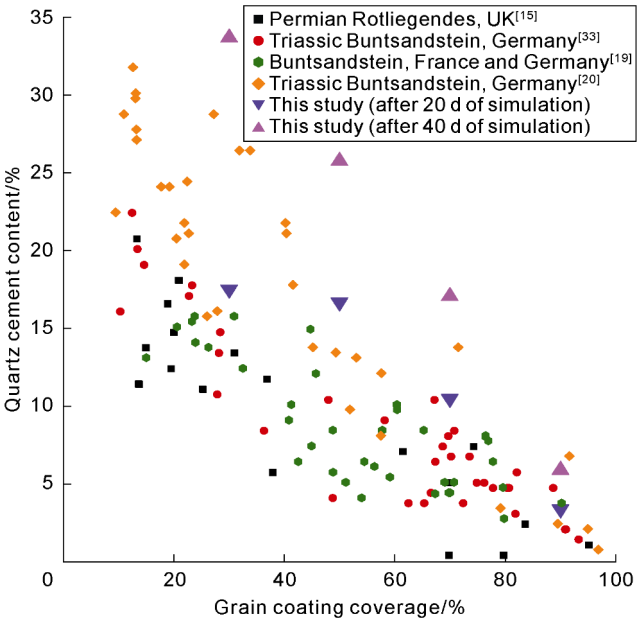

Fig. 11. Plot correlating the quartz cement content with grain coating coverages for different field samples and our simulation results after 20 d and 40 d.

"quartz plate" experiments of Lander et al. [10]. (2) The development of a novel digital pre-processing workflow to generate realistic clay coatings on quartz grains in multigrain packs, which enables us to simulate and analyze the impact of different coating parameters systematically.

Information about coating controls (i.e. orientation, coverage and pattern) is generally not available in field studies, and also does not exist in previous laboratory experiments and modeling literature. Through a series of overgrowth simulations on single grains and multi-grain packs, we uncovered important insights into the relative importance of these coating parameters.

Notably, the coverage of clay coatings emerges as the primary determinant of cement volume and growth rate, followed by the orientation of the crystallographic c-axis in relation to a clay coating and pattern. It is found that the growth rate of cement is lowest in the vertical orientation of quartz grain crystals, and the growth rate of coating is faster in the diagonal orientation than in the horizontal orientation at the middle-later stages of experiment. The influence of the coating pattern on cementation becomes more evident during later stages of diagenetic evolution of the reservoir, with faster cementation for layered coating pattern. The coating coverage is positively correlated with the porosity and permeability of sandstone.

The simulated overgrowths in multi-grain packs show clear similarities with natural samples, particularly in terms of how they encase clay coatings and occupy pore spaces, verifying the validity of the new approach of three-dimensional simulation on coating. Analysis of the numerical datasets generated from these simulations and examination of temporal evolution curves for cement volume, porosity, and permeability reveal valuable information about the dynamic changes in these reservoir properties occurring during the cementation process.

At same porosity, sandstones with higher coating percentage coverage exhibit higher permeability than those with lower coating coverage, due to the localized growth of overgrowths on uncoated grain surfaces, thereby facilitating unobstructed pore pathways.

Furthermore, the simulated quartz cement content, following equal exposure to supersaturated fluid for a duration of 20 d (simulation-time), exhibits good agreement with field samples, underscoring the reliability and accuracy of our simulation results.

The present study complements the previous works of Prajapati et al. [21–22]. Furthermore, this study contributes to the understanding of clay-coated sandstones and provides insights into reservoir property evolution. Looking ahead, the methodologies developed herein can be extended to other geological systems involving inert phases, such as quartz veins and calcite limestones, with relative ease. Moreover, as our model does not explicitly classify coatings as primary or diagenetic, we acknowledge this as an opportunity for future improvement. By leveraging these advancements, we can advance our understanding of reservoir dynamics and enhance the accuracy of reservoir characterization and prediction, ultimately benefiting various industries reliant on subsurface resource exploration and management.

Acknowledgments

We thank the Helmholtz association for funding the main parts of the modeling and simulation research work under the program “MTET: 38.04.04”. The authors acknowledge support by the state of Baden-Württemberg through bwHPC, and also thank Lukas Schöller from the Karlsruhe Institute of Technology for his assistance with generating digital grain packs and for the engaging discussions on the topic.

Nomenclature

a—gradient energy density function, J/m^4;

$a_{\mathrm{kin},\alpha\beta}(\hat{\boldsymbol{n}})$—dynamic anisotropy function at the α-β interface;

f_α—bulk free energy density of phase α, J/m^3;

f_{bulk}—bulk free energy density, J/m^3;

Δf_{ql}—driving force for quartz cementation, J/m^3;

F—Helmholtz free energy, J;

F_{bulk}—bulk free energy, J;

F_{intf}—interfacial free energy, J;

G—Gibbs function;

h—bulk free energy density interpolation function;

K—permeability, m^2;

k—a number between 1 to $n_{\alpha\beta}$;

$M_{\alpha\beta}(\hat{\boldsymbol{n}})$—mobility coefficient of the α-β interface, m^4/(J·s);

$M_{0,\mathrm{cl}}$—mobility coefficient of the clay-liquid interfacial kinetics, m^4/(J·s);

$M_{0,\alpha\beta}$—mobility coefficient of the α-β interfacial kinetics, $m^4/(J\cdot s)$;

N—number of phases;

$\hat{\boldsymbol{n}}$—unit vector orthogonal to the α-β interface;

$\boldsymbol{q}_{\alpha\beta}$—generalized phase-field gradient vector orthogonal to the α-β interface;

t—time, s;

Δt—time step, s;

t_{sim}—simulation time, s;

$\boldsymbol{u}$—liquid flow velocity vector, m/s;

$\bar{\boldsymbol{u}}$—average liquid flow velocity vector, m/s;

$\boldsymbol{x}$—position vector, m;

Δx, Δy, Δz—grid cell size, μm;

ϕ_α, ϕ_β, ϕ_γ—phase-field parameter of phases α, β, γ;

ϕ_{clay}—phase-field parameter of clay phase;

$\boldsymbol{\phi}(x,t)$—phase-field vector corresponding to position x and time t;

Ω—volume in physical domain, m^3;

ε—length, m;

ω—potential energy density function, J/m^2;

γ_{cc}—clay-clay interface energy density, J/m^2;

γ_{cl}—clay-liquid interface energy density, J/m^2;

γ_{ql}—quartz-liquid interface energy density, J/m^2;

γ_{qq}—quartz-quartz interface energy density, J/m^2;

$\gamma_{\alpha\beta}$—α-β interface energy density, J/m^2;

$\gamma_{\alpha\beta\delta}$—higher-order interface energy density, J/m^2;

$\boldsymbol{\eta}_{\alpha\beta}$—set of position vectors for the α-β interface anisotropy shape;

$\boldsymbol{\eta}_{\mathrm{cap},k}$—set of position vectors for the capillary anisotropy shape;

$\boldsymbol{\eta}_{\mathrm{kin},k}$—set of position vectors for the kinetic anisotropy shape;

μ_{d}—dynamic viscosity, Pa·s;

$\mu_{0,\mathrm{ql}}$—kinetic coefficient of the quartz-liquid interface, $m^4/(J\cdot s)$;

∇p—pressure gradient, Pa/m;

$\mathbb{R}_0^+$—non-negative real number set;

$\mathbb{R}^N$—a set of real number;

δ—kinetic anisotropy strength.

References

[1] AJDUKIEWICZ J M, LANDER R H. Sandstone reservoir quality prediction: The state of the art. AAPG Bulletin, 2010, 94(8): 1083–1091.

[2] HEALD M T, LARESE R E. Influence of coatings on quartz cementation. Journal of Sedimentary Research, 1974, 44(4): 1269–1274.

[3] PITTMAN E D, LARESE R E, HEALD M T. Clay coats: Occurrence and relevance to preservation of porosity in sandstones: HOUSEKNECHT D W, PITTMAN E D. Origin, Diagenesis, and Petrophysics of Clay Minerals in Sandstones. Tulsa: SEPM Society for Sedimentary Geology, 1992: 241–255.

[4] HOWARD J J. Influence of authigenic-clay minerals on permeability: HOUSEKNECHT D W, PITTMAN E D. Origin, diagenesis, and petrophysics of clay minerals in sandstones. Tulsa: SEPM Society for Sedimentary Geology, 1992: 257–264.

[5] AAGAARD P, JAHREN J S, HARSTAD A O, et al. Formation of grain-coating chlorite in sandstones. Laboratory synthesized vs. natural oc-currences. Clay Minerals, 2000, 35(1): 261–269.

[6] LIEWIG N, CLAUER N. K-Ar dating of varied microtextural illite in Permian gas reservoirs, northern Germany. Clay Minerals, 2000, 35(1): 271–281.

[7] ESCH W L, AJDUKIEWICZ J M, REYNOLDS A C. Early grain-coat formation in Chaco dune field, New Mexico: Insight into formation mechanisms, distribution, and implications for predictive modeling to assist in deep play identification. San Antonio: 2008 AAPG Annual Convention, 2008: 90078.

[8] BUSCH B. Pilot study on provenance and depositional controls on clay mineral coatings in active fluvio-eolian systems, western USA. Sedimentary Geology, 2020, 406: 105721.

[9] AJDUKIEWICZ J M, NICHOLSON P H, ESCH W L. Prediction of deep reservoir quality using early diagenetic process models in the Jurassic Norphlet Formation, Gulf of Mexico. AAPG Bulletin, 2010, 94(8): 1189–1227.

[10] LANDER R H, LARESE R E, BONNELL L M. Toward more accurate quartz cement models: The importance of euhedral versus noneuhedral growth rates. AAPG Bulletin, 2008, 92(11): 1537–1563.

[11] BLOCH S, LANDER R H, BONNELL L. Anomalously high porosity and permeability in deeply buried sandstone reservoirs: Origin and pre-dictability. AAPG Bulletin, 2002, 86(2): 301–328.

[12] WOOLDRIDGE L J, WORDEN R H, GRIFFITHS J, et al. How to quantify clay-coat grain coverage in modern and ancient sediments. Journal of Sedimentary Research, 2019, 89(2): 135–146.

[13] BUSCH B, HILGERS C, ADELMANN D. Reservoir quality controls on Rotliegend fluvio-aeolian wells in Germany and the Netherlands, Southern Permian Basin: Impact of grain coatings and cements. Marine and Petroleum Geology, 2020, 112: 104075.

[14] VERHAGEN I T E, CRISÓSTOMO-FIGUEROA A, UTLEY J E P. Abrasion of detrital grain-coating clays during sediment transport: Implications for diagenetic clay coats. Sedimentary Geology, 2020, 403: 105653.

[15] BUSCH B, HILGERS C, GRONEN L, et al. Cementation and structural diagenesis of fluvio-aeolian Rotliegend sandstones, northern England. Journal of the Geological Society, 2017, 174(5): 855–868.

[16] FRANKS S G, PANTANO J. A simple, effective petrographic method for quantifying percent clay or other grain-coat coverage in sandstones. Journal of Sedimentary Research,

2021, 91(2): 221–227.

[17] MONSEES A C, BUSCH B, SCHÖNER N, et al. Rock typing of diagenetically induced heterogeneities: A case study from a deeply-buried clastic Rotliegend reservoir of the Northern German Basin. Marine and Petroleum Geology, 2020, 113: 104163.

[18] MONSEES A C, BUSCH B, HILGERS C. Compaction control on diagenesis and reservoir quality development in red bed sandstones: A case study of Permian Rotliegend sandstones. International Journal of Earth Sciences, 2021, 110(5): 1683–1711.

[19] BUSCH B, ADELMANN D, HERRMANN R, et al. Controls on compactional behavior and reservoir quality in a Triassic Buntsandstein reservoir, Upper Rhine Graben, SW Germany. Marine and Petroleum Geology, 2022, 136: 105437.

[20] BUSCH B, BÖCKER J, HILGERS C. Improved reservoir quality assessment by evaluating illite grain coatings, quartz cementation, and com-paction: Case study from the Buntsandstein, Upper Rhine Graben, Germany. Geoenergy Science and Engineering, 2024, 241: 213141.

[21] PRAJAPATI N, SELZER M, NESTLER B, et al. Three-dimensional phase-field investigation of pore space cementation and permeability in quartz sandstone. Journal of Geophysical Research: Solid Earth, 2018, 123(8): 6378–6396.

[22] PRAJAPATI N, GONZALEZ A A, SELZER M, et al. Quartz cementation in polycrystalline sandstone: Insights from phase-field simulations. Journal of Geophysical Research: Solid Earth, 2020, 125(2): e2019JB019137.

[23] WENDLER F, OKAMOTO A, BLUM P. Phase-field modeling of epitaxial growth of polycrystalline quartz veins in hydrothermal experiments. Geofluids, 2016, 16(2): 211–230.

[24] SPÄTH M, URAI J L, NESTLER B. Formation of radiator structures in quartz veins-phase-field modeling of multicrack sealing. Journal of Structural Geology, 2022, 158: 104576.

[25] ANKIT K, URAI J L, NESTLER B. Microstructural evolution in bitaxial crack-seal veins: A phase-field study. Journal of Geophysical Research: Solid Earth, 2015, 120(5): 3096–3118.

[26] SPÄTH M, SPRUŽENIECE L, URAI J L, et al. Kinematics of crystal growth in single-seal syntaxial veins in limestone: A phase-field study. Journal of Geophysical Research: Solid Earth, 2021, 126(10): e2021JB022106.

[27] PRAJAPATI N, SELZER M, NESTLER B. Computational modeling of calcite cementation in saline limestone aquifers: A phase-field study. Geothermal Energy, 2017, 5(1): 15.

[28] PRAJAPATI N, SPÄTH M, KNECHT L, et al. Quantitative phase-field modeling of faceted crystal dissolution processes. Crystal Growth & Design, 2021, 21(6): 3266–3279.

[29] KUMAR A, PRAJAPATI N, SPÄTH M, et al. Qualitative dissolution modeling of etch-pit formation on the K-feldspar surface through phase-field approach. Journal of Geophysical Research: Solid Earth, 2023, 128(4): e2022JB025749.

[30] TAMBURELLI S, DI GIULIO A, AMADORI C, et al. New constraint on burial and thermal history of Devonian reservoir sandstones in the Illizi-Ghadames Basin (North Africa) through diagenetic numerical modelling. Marine and Petroleum Geology, 2022, 145: 105903.

[31] SPRUŽENIECE L, SPÄTH M, URAI J L, et al. Wide-blocky veins explained by dependency of crystal growth rate on fracture surface type: Insights from phase-field modeling. Geology, 2021, 49(6): 641–646.

[32] HÖTZER J, REITER A, HIERL H, et al. The parallel multi-physics phase-field framework PACE3D. Journal of Computational Science, 2018, 26: 1–12.

[33] BUSCH B, SPITZNER A D, ADELMANN D, et al. The significance of outcrop analog data for reservoir quality assessment: A comparative case study of Lower Triassic Buntsandstein sandstones in the upper Rhine graben. Marine and Petroleum Geology, 2022, 141: 105701.

[34] BUSCH B, OKAMOTO A, GARBEV K, et al. Experimental fracture sealing in reservoir sandstones and its relation to rock texture. Journal of Structural Geology, 2021, 153: 104447.

[35] MANNING C E. The solubility of quartz in H_2O in the lower crust and upper mantle. Geochimica et Cosmochimica Acta, 1994, 58(22): 4831–4839.

[36] SANJUAN B, MILLOT R, INNOCENT C, et al. Major geochemical characteristics of geothermal brines from the Upper Rhine Graben granitic basement with constraints on temperature and circulation. Chemical Geology, 2016, 428: 27–47.

[37] NESTLER B, GARCKE H, STINNER B. Multicomponent alloy solidification: Phase-field modeling and simulations. Physical Review E, 2005, 71(4): 041609.

[38] STEINBACH I. Phase-field models in materials science. Modelling and Simulation in Materials Science and Engineering, 2009, 17(7): 073001.

[39] KUMAR A, SPÄTH M, PRAJAPATI N, et al. Dataset for phase-field simulation showcasing impact of clay-coating on sandstone reservoir. (2024-06-07)[2024-10-10]. https://doi.org/10.5281/ zenodo.11506190.

[40] CHARLAFTIS D, DOBSON K J, JONES S J, et al. Experimental simulation of burial diagenesis and subsequent 2D-3D characterization of sandstone reservoir quality. Frontiers in Earth Science, 2022, 10: 766145.

[41] WARREN E A, SMALLEY C P, HOWARTH R. Part 4: Compositional variations of North Sea formation waters. Geological Society, London, Memoirs, 1994, 15(1): 119–208.

[42] SARI A, AL MASKARI N S, SAEEDI A, et al. Impact of surface roughness on wettability of oil-brine-calcite system at sub-pore scale. Journal of Molecular Liquids, 2020, 299: 112107.

[43] SPÄTH M, SELZER M, BUSCH B, et al. Phase-field simulations of epitaxial crystal growth in open fractures with reactive lateral flow. Water Resources Research, 2023, 59(8): e2023WR034605.